

Nonlocal imaging by conditional averaging of random reference measurements

LUO Kai-Hong ¹, HUANG Boqiang ¹, ZHENG Wei-Mou ², and WU Ling-An ^{1*}

¹Laboratory of Optical Physics, Institute of Physics and Beijing National Laboratory for Condensed Matter Physics, Chinese Academy of Sciences, Beijing 100190, China

²Institute of Theoretical Physics, Chinese Academy of Sciences, Beijing 100190, China

(Dated: 20 June 2012)

We report the nonlocal imaging of an object by conditional averaging of the random exposure frames of a reference detector, which only sees the freely propagating field from a thermal light source. A bucket detector, synchronized with the reference detector, records the intensity fluctuations of an identical beam passing through the object mask. These fluctuations are sorted according to their values relative to the mean, then the reference data in the corresponding time-bins for a given fluctuation range are averaged, to produce either positive or negative images. Since no correlation calculations are involved, this correspondence imaging technique challenges our former interpretations of “ghost” imaging. Compared with conventional correlation imaging or compressed sensing schemes, both the number of exposures and computation time are greatly reduced, while the visibility is much improved. A simple statistical model is presented to explain the phenomenon.

PACS numbers: 42.50.Ar, 42.30.Va, 42.50.St

Classical image formation is most commonly realized by recording the interaction information between a radiation source and the object onto a detector, all along a single light path. However, in the technique now known as “ghost” imaging (GI), two beams are used from the same optical source; one beam interacts with the target and is collected by a so-called “bucket” detector which has no spatial resolution and only measures the total intensity, while the other propagates through free space to a reference detector which does have spatial resolution. Neither detector can “see” the object on its own, but when their second-order correlation is measured, the image appears in the coincidence data. This seems quite contrary to intuition, and after the first experiment was demonstrated with entangled twin beams [1], the term “ghost” was coined to emphasize its peculiar nonlocal nature, which was attributed to the quantum properties of the biphoton source. Because of the potential applications, interest soon spread to other sources [2], followed by a profusion of studies on GI with pseudothermal light [3–8], true thermal light [9], and even GI without a lens [10–15]. The expression “nonlocal imaging” is now understood to mean that the light recorded by the reference detector travels through free space and never interacts with the object, and is still generally accepted in the GI community irrespective of whether the source is quantum or classical. Since the prerequisite for correlated imaging is the identical spatial distribution of the field intensities in the two beams, it was then realized that the reference beam could just as well be replaced by an artificially generated random spatial modulation of the object beam, thus only a bucket detector would be necessary. After the experimental demonstration of this kind of computational ghost imaging [16, 17], atten-

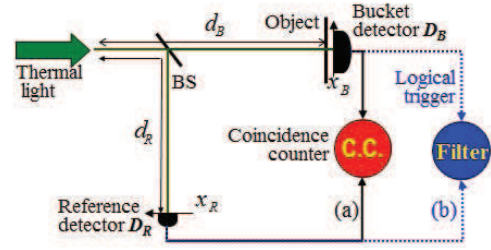


FIG. 1: Schematic of correlated imaging. BS: beamsplitter. (a) Conventional GI; (b) Correspondence imaging with selected reference information.

tion turned to improving the techniques involved in the data collection, correlation and averaging of thousands of exposure frames. Compressed sensing was found to be very effective in greatly reducing the number of frames required when the image data is sparse, and has already been implemented [18].

Despite all these advances, there is still much debate on the various quantum and classical interpretations of GI [16, 19]. Basically, two different interpretations have been offered: one is multi-photon interference based on Glauber’s quantum optical coherence, and the other is intensity fluctuation correlation. From the point of view of image processing, the key to GI reconstruction is the extraction of information according to the time correspondence between the bucket signals and reference frames. From the mathematical viewpoint, the image retrieval is akin to an inverse problem in which the features (pixels) of an object are to be inferred, given a time series of bucket and reference light field intensities.

The basic scheme of a correlated GI system is shown in Fig. 1(a). Thermal (or entangled) light is separated into two parts through a beamsplitter (BS). An object characterized by the transmission function $T(\vec{x}_0)$, where \vec{x}_0 indicates the transverse coordinate in the plane of the object, is inserted in front of a bucket detector D_B (without

*Corresponding author: wula@aphy.iphy.ac.cn

any spatial resolution), which registers the total intensity I_B transmitted (or reflected) by the object, while a reference detector D_R with spatial resolution is in the other empty arm. The distances from the source to the object and to D_R are d_B and d_R , respectively. For lensless GI with thermal light, the phase-conjugate mirror requirement $d_B = d_R$ must be satisfied [7, 10]. In conventional GI, an image of the mask is retrieved from the coincidence measurements of D_B and D_R when the latter is scanned in the corresponding image plane, so all the information from both the detectors is required. The basis of GI is the transverse spatial second-order correlation[20]

$$G^{(2)}(\vec{x}_B, \vec{x}_R) = \frac{1}{N} \sum_{\{t_i | i=1, \dots, N\}} I_B(\vec{x}_B, t_i) I_R(\vec{x}_R, t_i) \quad (1)$$

Here $I_B(\vec{x}_B, t_i)$, $I_R(\vec{x}_R, t_i)$ and \vec{x}_B, \vec{x}_R are the intensities at time t_i and the transverse coordinates at D_B and D_R , respectively; N is the number of the coincidence measurements, i.e. exposure frames. The output $I_B(t_i)$ of the bucket detector is the spatial integral $\int d\vec{x}_B I_B(\vec{x}_B, t_i)$, which erases the spatial resolution of the target.

Below, we demonstrate a method using incoherent thermal light by which an image of the object can be obtained very simply from the raw reference detector data, without the need of any complicated image reconstruction method such as that based on compressed sensing [21]. In this method, which we shall call correspondence imaging (CI), we only have to perform signal averaging over those reference frames selected by an appropriate gate from the bucket detector. Since no direct second-order correlation is involved, the theory seems to challenge all our previous interpretations of GI. In addition to the normal positive image, a reversed negative image can also be obtained, and the quality of the images may be far superior to that of conventional GI for the same number of frames.

A schematic of the CI setup is shown in Fig. 1(b). As in (a), a linearly polarized He-Ne laser beam diameter 5 mm is projected onto a rotating ground-glass disk to produce pseudothermal light [22], which is then split by a 50:50 non-polarizing BS into two beams, one of which passes through an object mask to detector D_B , and the other goes directly to D_R , to produce the bucket intensity I_B and the reference intensity distribution $I_R(\vec{x}_R)$, respectively. The distance from the ground-glass disk to BS is 19 cm, and from BS to the mask 11 cm, that is, $d_B = d_R \sim 30$ cm. Both detectors (Imaging Source DMK 31BU03) are synchronized by the same trigger pulse at a rate of about 3 Hz. The data was acquired with an exposure time (0.1 ms) much shorter than the coherence time of the laser, and saved to a computer. A total of 50,000 frames was grabbed by each camera per image plot. The bucket detector could also be just a point detector so long as it collects all the light transmitted through the mask, for example by means of a focusing lens.

The integrated beam intensity $I_B(t_i)$ at the bucket detector recorded as a function of time is shown in Fig. 2(a);

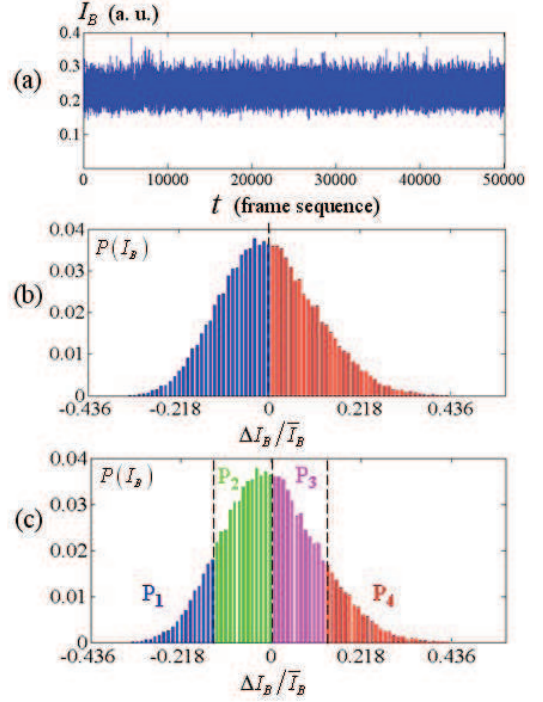


FIG. 2: Bucket detector intensity I_B . (a) Integrated beam intensity I_B recorded as a function of time sequence. (b) Probability distribution of I_B centered about its mean. The left (blue) block is binned for $\Delta I_B < 0$, and the right (red) block for $\Delta I_B \geq 0$. The dashed line denotes \bar{I}_B . (c) Multi-section binning. From left to right, the dashed lines denote I_N , \bar{I}_B and I_P , where I_N and I_P satisfy $P(I_N) = P(I_P) = P(\bar{I}_B)/2$.

it can be seen that the intensity fluctuations are random. We then calculate the deviation from the mean $\Delta I_B(t_i) = I_B(t_i) - \bar{I}_B$, and plot the histogram of $I_B(t_i)$, or equivalently of the normalized intensity fluctuations $\Delta I_B(t_i)/\bar{I}_B$, to show the probability distribution $P(I_B)$ of I_B . Using the intensity $I_B(t_i)$ at time t_i as an indicator, we divide $\{t_i\}$ into two subsets:

$$t_- = \{t_i | I_B(t_i) < \bar{I}_B\}, \quad t_+ = \{t_i | I_B(t_i) \geq \bar{I}_B\}. \quad (2)$$

All the $I_B(t_i)$ with $t_i \in t_-$ (or t_+) contribute to the left (or right) half of Fig. 2(b).

Because both detectors are synchronized in time, the reference signals $I_R(\vec{x}_R, t_i)$ may also be divided into two groups according to $t_i \in t_+$ or $t_i \in t_-$. This is equivalent to labeling $I_R(\vec{x}_R, t_i)$ with the time stamp of $I_B(t_i)$. By dividing the range of I_B into more sections, say at I_N and I_P as well as at \bar{I}_B , with $\Delta I_N < 0$, $\Delta I_P > 0$, and $P(I_N) = P(I_P) = P(\bar{I}_B)/2$, we can perform multi-section binning for I_B (Fig. 2(c)), and hence, correspondingly, for $I_R(\vec{x}_R, t_i)$.

Due to the free propagation of the thermal light field, each reference frame is purely random, so the average

value of all the reference signals is

$$\bar{I}_R(\vec{x}_R) = \frac{1}{N} \sum_{\{t_i|i=1,\dots,N\}} I_R(\vec{x}_R, t_i) = \bar{I}_R. \quad (3)$$

Statistically, the mean value of a random variable is a constant, so we would not expect $\bar{I}_R(\vec{x}_R)$ to reveal anything, however long the exposure time, as shown in Fig. 3(a), and for a homogeneous thermal field each pixel would have the same averaged intensity. But amazingly, after the above partitioning, the target in the object arm can be reconstructed merely by taking the average of only the reference intensities within a selected distribution:

$$R_{\pm}(\vec{x}_R) = \frac{1}{N_{\pm}} \sum_{\{t_i|t_i \in t_{\pm}\}} I_R(\vec{x}_R, t_i), \quad (4)$$

where $N_{\pm} = \sum_{t_i \in t_{\pm}} 1$ is the cardinality of t_{\pm} (see Figs. 3(b) and (c)).

We know from information theory and statistics that a complete random basis is recommended for image reconstruction. In our experiment this is supplied by the spatial fluctuations of all the random modes of the thermal beams. The object and D_R are at the same distance from the source, so they see the same mode distribution. Part of this field, i.e. the transmitted (or reflected) light through the mask, contributes to the bucket signal, and may fluctuate above or below its mean value in each exposure. The intensity of the corresponding D_R pixels will also fluctuate in harmony, but the rest of the frame will be fluctuating in an uncorrelated way. Let us divide the spatial pixels at the mask $\{\vec{x}_0\}$ into subsets X_1 and X_0 with the former transmitting and the latter blocking light. It is the pixels $\{\vec{x}_0 | \vec{x}_0 \in X_1\}$ that contribute to the bucket signal I_B , and when the field intensity fluctuates higher (lower) in this area, the bucket output will naturally increase (decrease). The intensity of the corresponding reference detector pixels will also increase (decrease), but as this contribution is superimposed upon the entire beam intensity, i.e. all the light from both areas X_1 and X_0 , the total reference output will be more or less constant. By separately collecting and averaging over a sufficiently large number of exposures according to the positive (negative) bucket signals, the positive (negative) image of the object (X_1) will then stand out from the constant background.

A conceptual mathematical model is as follows. Since the field distribution at the mask is the same as that at D_R , the bucket intensity may be written

$$I_B(t_i) = \sum_{\{\vec{x}\}} I_R(\vec{x}, t_i) |T(\vec{x})|^2, \quad (5)$$

where for convenience we have dropped the subscripts of x . From Eq. (3) we thus have $\bar{I}_B = \bar{I}_R \sum_{\{\vec{x}\}} |T(\vec{x})|^2$.

For a narrow bucket intensity bin, centered at some $I_B(t_i) \approx I_B^+$ far above \bar{I}_B , we may make the following approximation

$$I_B(t_i) \simeq \sum_{\{\vec{x}|\vec{x} \in X_1\}} I_R(\vec{x}, t_i) |T(\vec{x})|^2. \quad (6)$$

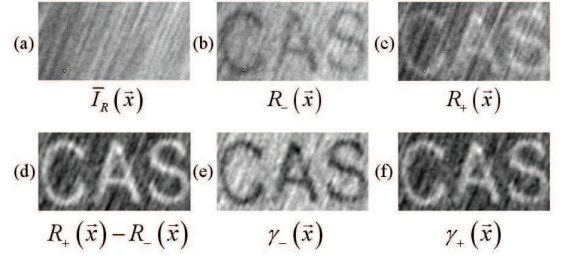


FIG. 3: Images obtained by nonlocal CI; all figures are automatically gray-scale compensated. (a) Average of all the frames from D_R . (b) Negative and (c) positive correspondence images after time binning of D_R based on negative and positive ΔI_B , respectively. (d) Images obtained using all the frames from D_R but with the negative image signals $R_-(\vec{x})$ inverted. (e) and (f), as in (b) and (c) above, respectively, but after normalized array division by (a).

Since N_{B+} is the number of $I_B(t_i)$ values registered in the range of I_B^+ , we can write

$$\begin{aligned} G_+(\vec{x}) &\equiv \frac{1}{N_{B+}} \sum_{\{t_i|I_B(t_i) \approx I_B^+\}} I_B(t_i) I_R(\vec{x}, t_i) \\ &\simeq \frac{I_B^+}{N_{B+}} \sum_{\{t_i|I_B(t_i) \approx I_B^+\}} I_R(\vec{x}, t_i) \equiv \frac{I_B^+}{N_B^+} I^+(\vec{x}) \end{aligned} \quad (7)$$

On the other hand, by using Eq. (5), we have

$$G_+(\vec{x}) \simeq \bar{I}_B \bar{I}_R + \Delta_R^2 |T(\vec{x})|^2, \quad (8)$$

where $\Delta_R^2 = \frac{1}{N_{B+}} \sum_{\{t_i|I_B(t_i) \approx I_B^+\}} [I_R(\vec{x}, t_i) - \bar{I}_R]^2$. This means that, for $\vec{x} \in X_1$

$$I^+(\vec{x}) \propto C_b + |T(\vec{x})|^2, \quad (9)$$

with $C_b = \bar{I}_B \bar{I}_R / \Delta_R^2$ being a constant due to the background. Similarly, for $\vec{x} \in X_0$ we have $I^+(\vec{x}) \propto C_b + 0$. For a narrow bin centered at some I_B^- far below I_B , the same argument is applicable under the exchange $X_1 \leftrightarrow X_0$. Thus, while the summation of reference frames corresponding to $I_B(t_i) \approx I_B^+$ gives the positive image of pixels in X_1 , the summation frames for $I_B(t_i) \approx I_B^-$ gives the negative image of pixels in X_0 .

When going from the narrow bin at I_B^+ to a wide bin of $I_B(t_i) \geq \bar{I}_B$, errors from two sources come in: since $I_B(t_i) \geq \bar{I}_B$ is approximated by the single value I_B^+ , the validity of Eq. (6) becomes weaker. This implies that the reference frames with their corresponding $I_B(t_i)$ close to \bar{I}_B contain limited information about $|T(\vec{x})|^2$, relative to the background, so the image quality is reduced. However, if we take $R_+(\vec{x}) - R_-(\vec{x})$ then the background can be removed. We may also define the normalized distributions $\gamma_{\mp}(\vec{x}) = R_{\mp}(\vec{x}) / \bar{I}_R(\vec{x})$.

Figure 3 shows the images obtained for the letters ‘‘CAS’’ in an object mask which is 1.4×2.56 mm² in size (300×550 pixels). We define two levels of transmission,

1 for total transmission through the letters, and 0 elsewhere. The results obtained by various different methods are presented for comparison to illustrate the advantages of CI. We see from Fig. 3(a) that, as expected, merely taking the time average $\bar{I}_R(\vec{x})$ using all the 50,000 frames of the reference detector produces nothing (the slanted lines are artifacts from the rotating ground glass plate due to the long time exposures). After partitioning by the two complementary time series given by Eq. (2), there emerges a negative image $R_-(\vec{x})$ from 26,005 reference frames (Fig. 3(b)), and a positive image $R_+(\vec{x})$ from the remaining frames (Fig. 3(c)). The image $R_+(\vec{x}) - R_-(\vec{x})$ obtained using all the information from D_R but with the negative image signals inverted is shown in Fig. 3(d). When we take the normalized correspondence images from D_R , obtained as $\gamma_-(\vec{x})$ and $\gamma_+(\vec{x})$ by using matrix array division, we obtain the images in (e) and (f), respectively, which are much clearer than in (b) and (c) above. It is interesting to note that in all the upper row figures, there is a small black dot with a white centre at the bottom of the letter “C”, due to diffraction from a dust particle on the surface of the reference detector. However, this is no longer visible in the lower row as the background has been removed through normalization.

It should be noted that although CI still requires synchronization with the bucket detector signals, it is quite different from the usual correlated imaging of GI. Each individual frame of D_R is random and the object cannot be seen from the mean of the total, but its image can be retrieved from the conditional average of subsets of the data, a seeming contradiction. Moreover, the visibility of the images may be optimized by appropriate selection and weighting of the data partitioning, for example, through appropriate choice of bucket detector intensities I_N and I_P , we can divide the histogram into four areas, as illustrated in Fig. 2(c). Besides \bar{I}_B , we introduce two more $I_N (< \bar{I}_B)$ and $I_P (> \bar{I}_B)$ to divide the range of I_B into four subintervals: $P_1 = [0, I_N)$, $P_2 = [I_N, \bar{I}_B)$, $P_3 = [\bar{I}_B, I_P)$, and $P_4 = [I_P, +\infty)$. Assuming that there are N_i measurements (or frames) with a bucket intensity within the range P_i ($i = 1, 2, 3, 4$), in the same way as we defined $R_{\mp}(\vec{x})$, we introduce

$$R_i(\vec{x}) = \frac{1}{N_i} \sum_{\{t_i | I_B(t_i) \in P_i\}} I_R(\vec{x}, t_i), \quad (10)$$

and its normalized form $\gamma_i(\vec{x}) = R_i(\vec{x})/\bar{I}_R(\vec{x})$. We expect that a negative image would be obtained with R_1 or R_2 and a positive image with R_3 or R_4 .

Using the same experimental data as above, three sets of values for N_i were chosen to create the correspondence images of Fig. 4. In the first row, the number of reference frames contained in each sector P_i was the same ($N_1 \sim N_2 \sim N_3 \sim N_4$). It is obvious that the images obtained from P_1 and P_4 are far superior in quality compared to those from P_2 and P_3 , although the same number of frames were used. In the second row, a weighting of $N_1 : N_2 : N_3 : N_4 \sim 1 : 9 : 9 : 1$ was used. Even

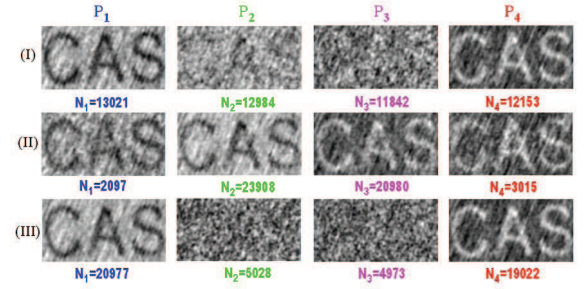


FIG. 4: Selected CI images when the information from D_R is divided into four subsets with different weightings (the gray-scale has been automatically adjusted). (I) Each subset is composed of the same number of measurements, $N_1 \sim N_2 \sim N_3 \sim N_4$; (II) most of the frames are concentrated in the central areas P_2 and P_3 , with a weighting of $N_1 : N_2 : N_3 : N_4 \sim 1 : 9 : 9 : 1$; (III) when $N_1 : N_2 : N_3 : N_4 \sim 4 : 1 : 1 : 4$, no images can be deciphered from P_2 and P_3 .

in this case, we see that the reconstructions from the extrema, i.e. the wings of the fluctuation distributions in Figs. 2(b) and (c), are comparable with those from the central area, despite the fact that only 5% of the data was used. In the third row, the ratios of the four parts are about $N_1 : N_2 : N_3 : N_4 \sim 4 : 1 : 1 : 4$, and we can no longer see any image in the regions of P_2 and P_3 . This indicates that most of the object information is concentrated at the two ends P_1 and P_4 , i.e., the reference frames corresponding to larger bucket intensity fluctuations contain more information and contribute more to image retrieval. When the image is indistinguishable from the background, we may infer that the exposure intensities resulted from both subsets X_1 and X_0 . By refining our weighting of the partition selection, the image may be recovered faster and with fewer measurements, in agreement with the experimental observations of Fig. 4.

It should be noted that in Figs. 3 and 4 the gray-scale has been automatically adjusted by the software for better pictorial detail: the minimum of the image matrix is displayed as the darkest and the maximum as the brightest so that contrast is artificially improved. In this way, images that originally had very different visibilities may look quite similar on a computer screen, or vice versa. The CI images appear comparable to those obtained by conventional GI although only half the data from D_R or even less is used.

To demonstrate the superior visibility of CI more clearly we also performed an experiment under the same conditions as before but with a simple double-slit as object (slit width and distance 0.2 mm and 0.4 mm, respectively). The fluctuation histogram of I_B was divided into four sectors, and to spotlight the differences in visibility we look at the intensity profiles along one transverse dimension. For a better comparison of the original image contrast of the various techniques, in Fig. 5 we have adopted a common gray-scale in which the image matrices are divided by their maximum value and dis-

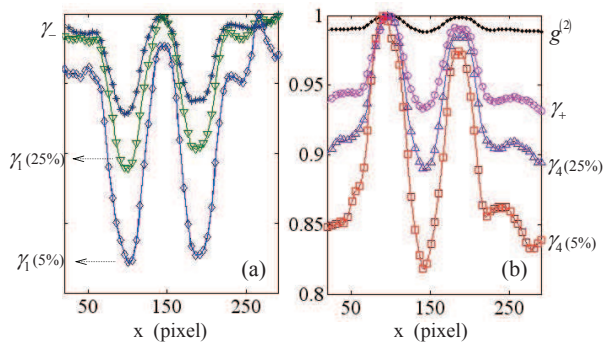


FIG. 5: Image intensity profiles for a double-slit object; transverse coordinates are the pixels of D_R (each pixel is 4.65 by $4.65 \mu\text{m}^2$). Each plot is normalized by its maximum value. (a) Normalized negative correspondence images reconstructed for γ_- and two γ_1 values. (b) Top curve: second-order normalized GI; lower three curves: normalized correspondence images reconstructed for γ_+ and two γ_4 values.

played with zero as the darkest and 1 as the brightest. Fig. 5(a) shows the normalized negative correspondence images, where γ_- indicates the negative image when the probability histogram is only divided into two parts, and the percentage values in $\gamma_1(25\%)$ and $\gamma_1(5\%)$ represent the percentage N_1 of reference frames selected in partition P_1 . Fig. 5(b) shows positive images: the top curve is from normalized second-order correlation GI; γ_+ is the normalized positive CI image, and $\gamma_4(25\%)$ and $\gamma_4(5\%)$ are the CI plots for $N_4/N \simeq 25\%$ and 5% . The superiority of the latter is immediately obvious. Moreover, the less the number of exposures that are taken, the better is the visibility relative to that in conventional GI. The definition and analysis of the visibility and signal-to-noise ratio in CI is a complicated problem [23, 24], so a more

quantitative discussion, as well as a full theory of CI in general, will be presented in a future paper.

In summary, we have demonstrated the reconstruction of positive and negative images of a nonlocal object through selective averaging of the exposures of a reference detector that has never interacted with the target field. A simple statistical model is proposed to explain the phenomenon, which, to our knowledge, cannot be explained by conventional classical or quantum wave optics. Since the method is based on a form of conditional averaging of the reference data, much less information is required than in GI, which in fact contains much redundant information. Moreover, the visibility is significantly better, especially if the number of exposure frames is limited. The reconstruction process only involves straightforward selection and stacking, so it is much simpler than conventional GI or compressed sensing methods; complicated calculations and algorithms are not required, and storage space, memory consumption and processing time are greatly reduced, which is a particular advantage when the images are large. The basic concept may also be extended to similar experiments that use correlation calculation, including computational GI, so potential applications are plentiful. Although this CI technique is apparently simple, the underlying physics is quite subtle and deserves further exploration. It could open up new opportunities in the field of metrology, positioning, and imaging.

This work was supported by the National Natural Science Foundation of China Grant No. 60978002, the National Program for Basic Research in China Grant Nos. 2010CB922904 and 2007CB814800, and the National High Technology R & D Program of China Grant No. 2011AA120102.

-
- [1] Pittman T B, Shih Y H, Strekalov D V and Sergienko A V 1995 *Phys. Rev. A* **52** 3429(R)
 - [2] Cheng J and Han S S 2004 *Phys. Rev. Lett.* **92** 093903
 - [3] Bennink R S, Bentley S J and Boyd R W 2002 *Phys. Rev. Lett.* **89**, 011360; Bennink R S, Bentley S J, Boyd R W and Howell J C 2004 *Phys. Rev. Lett.* **92** 033601
 - [4] Gatti A, Brambilla E, Bache M and Lugiato L A 2004 *Phys. Rev. Lett.* **93** 093602
 - [5] Ferri F, Magatti D, Gatti A, Bache M, Brambilla E and Lugiato L A 2005 *Phys. Rev. Lett.* **94** 183602
 - [6] Cai Y J and Zhu S Y 2005 *Phys. Rev. E* **71** 056607
 - [7] Cao D Z, Xiong J and Wang K G 2005 *Phys. Rev. A* **71** 013801
 - [8] Valencia A, Scarcelli G, D'Angelo M and Shih Y 2005 *Phys. Rev. Lett.* **94** 063601
 - [9] Zhang D, Zhai Y H, Wu L A and Chen X H 2005 *Opt. Lett.* **30** 2354
 - [10] Scarcelli G, Berardi V and Shih Y H 2006 *Appl. Phys. Lett.* **88** 061106
 - [11] Basano L and Ottonello P 2006 *Appl. Phys. Lett.* **89** 091109
 - [12] Meyers R, Deacon K S and Shih Y H 2008 *Phys. Rev. A* **77** 041801(R)
 - [13] Liu H L and Han S S 2008 *Opt. Lett.* **33** 824
 - [14] Ferri F, Magatti D, Sala V G and Gatti A 2008 *Appl. Phys. Lett.* **92** 261109
 - [15] Chen X H, Liu Q, Luo K H and Wu L A 2009 *Opt. Lett.* **34** 695
 - [16] Shapiro J H 2008 *Phys. Rev. A* **78** 061802(R); Erkmen B I and Shapiro J H 2010 *Advances in Optics and Photonics* **2** 405
 - [17] Bromberg Y, Katz O and Silberberg Y 2009 *Phys. Rev. A* **79** 053840
 - [18] Katz O, Bromberg Y and Silberberg Y 2009 *Appl. Phys. Lett.* **95** 131110
 - [19] Shih Y 2007 *IEEE J. Sel. Top. Quantum Electronics* **13** 1016
 - [20] Glauber R J 1963 *Phys. Rev.* **131** 2766
 - [21] Wu L A and Luo K H 2011 *AIP Conf. Proc.* **1384** 223
 - [22] Goodman J W *Statistical Optics* (Wiley Classic Library,

- New York, 2000); Goodman J W *Speckle Phenomena in Optics: Theory and Applications* (Roberts & Company (Englewood, Colorado), 2007)
- [23] Basano L and Ottonello 2007 *Appl. Opt.* **46** 6291
- [24] Brida G, Chekhova M V, Fornaro G A, Genovese M, Lopaeva E D and Ruo Berchera I 2011 *Phys. Rev. A* **83** 063807